A novel micro-ECoG recording method for recording multisensory neural activity from the parietal to temporal cortices in mice

Susumu Setogawa[1,2], Ryota Kanda[3], Shuto Tada[3], Takuya Hikima[1], Yoshito Saitoh[1], Mikiko Ishikawa[1], Satoshi Nakada[4], Fumiko Seki[5], Keigo Hikishima[6], Hideyuki Matsumoto[2], Kenji Mizuseki[2], Osamu Fukayama[7], Makoto Osanai[8], Hiroto Sekiguchi[3,9,*], and Noriaki Ohkawa[1,*]

[1] Division for Memory and Cognitive Function, Research Center for Advanced Medical Science, Comprehensive Research Facilities for Advanced Medical Science, Dokkyo Medical University, Tochigi 321-0293, Japan

[2] Department of Physiology, Osaka Metropolitan University Graduate School of Medicine, Osaka 545-8585, Japan

[3] Department of Electrical and Electronic Information Engineering, Toyohashi University of Technology, Toyohashi, Aichi 441-8580, Japan

[4] Japanese Center for Research on Women in Sport, Juntendo University Graduate School of Health and Sports Science, Chiba 270-1695, Japan.

[5] Live Animal Imaging Center, Central Institutes for Experimental Animals (CIEA),

Kanagawa 210-0821, Japan

[6] Medical Devices Research Group, Health and Medical Research Institute, National Institute of Advanced Industrial Science and Technology (AIST), Tsukuba 305-8564, Japan.

[7] Information and Neural Networks Lab, Center for Information and Neural Networks (CiNet), National Institute of Information and Communications Technology, Suita, Osaka 565-0871, Japan

[8] Laboratory for Physiological Functional Imaging, Department of Medical Physics and Engineering, Division of Health Sciences, Osaka University Graduate School of Medicine, Suita, Osaka 565-0871, Japan

[9] Japan Science and Technology, Precursory Research for Embryonic Science and Technology (PRESTO), Kawaguchi, Saitama 332-0012, Japan.

*Address for correspondence:

Noriaki Ohkawa, Ph.D

Division for Memory and Cognitive Function, Research Center for Advanced Medical Science, Comprehensive Research Facilities for Advanced Medical Science, Dokkyo

Medical University, Tochigi 321-0293, Japan

E-mail: nohkawa@dokkyomed.ac.jp

Tell: +81-282-87-2478

Hiroto Sekiguchi, Ph.D

Department of Electrical and Electronic Information Engineering, Toyohashi University of Technology, Toyohashi, Aichi 441-8580, Japan

E-mail: sekiguchi@ee.tut.ac.jp

Tell: +81-532-44-6744

Abstract

Characterization of inter-regional interactions in brain is essential for understanding the mechanism relevant to normal brain function and neurological disease. The recently developed flexible micro (μ)-electrocorticography (μECoG) device is one prominent method used to examine large-scale cortical activity across multiple regions. The sheet-shaped μECoG electrodes arrays can be placed on a relatively wide area of cortical surface beneath the skull by inserting the device into the space between skull and brain. Although rats and mice are useful tools for neuroscience, current μECoG recording methods in these animals are limited to the parietal region of cerebral cortex. Recording cortical activity from the temporal region of cortex in mice has proven difficult because of surgical barriers created by the skull and surrounding temporalis muscle anatomy. Here, we developed a sheet-shaped 64-channel μECoG device that allows access to the mouse temporal cortex, and we determined the factor determining the appropriate bending stiffness for the μECoG electrode array. We also established a surgical technique to implant the electrode arrays into the epidural space over a wide area of cerebral cortex covering from the barrel field to olfactory (piriform) cortex, which is the deepest region of the cerebral cortex. Using histology and computed tomography (CT) images, we confirmed that the tip of the μECoG device reached to the most ventral part of cerebral

cortex without causing noticeable damage to the brain surface. Moreover, the device simultaneously recorded somatosensory and odor stimulus-evoked neural activity from dorsal and ventral parts of cerebral cortex in awake and anesthetized mice. These data indicate that our μECoG device and surgical techniques enable the recording of large-scale cortical activity from the parietal to temporal cortex in mice, including somatosensory and olfactory cortices. This system will provide more opportunities for the investigation of physiological functions from wider areas of the mouse cerebral cortex than those currently available with existing ECoG techniques.

(309 words)

Key Words

Electrocorticography, flexible micro-electrocorticography device, Multi-sensory, Cerebral cortex, Temporal cortex, Local Field Potential

Introduction

Neural networks in the cerebral cortex are composed of functionally different regions which process information from distinct modalities to drive cognitive functions including attention, learning, and memory. Altered network activity from multiple cortical regions is linked to neurological disorders, such as seizure, dementia, and schizophrenia [1-3]. Therefore, characterization of inter-cortical interactions is essential for understanding the mechanisms underlying normal cognitive functions and neuropathology.

Methods in neuroscience, such as large-scale calcium imaging, electroencephalography (EEG), and electrocorticography (ECoG), enable the monitoring of neural activity from a wide area of cerebral cortex, providing insight into inter-regional cortical network interactions [4-6]. These techniques, combined with rodent experiments and a variety of genetic tools, have contributed to advances in neuroscience[7]. However, the measurement area of current large-scale calcium imaging and electrophysiological techniques focusing on cerebral cortex has been mostly limited to parietal regions, including sensorimotor, visual, auditory, parietal, and retrosplenial cortices [5, 8, 9]. A major reason for the limitation in measurement area is the difficulty in the associated operation, since the temporal region of the cortex is covered by skull surrounded with

100 temporalis muscles [10]. Moreover, the most common methods that use head fixation in
101 rats and mice, such as the ear bars used in craniotomy and the head-fixation plate[11],
102 interferes with microscopy and electrode implantation for large-scale recordings of the
103 temporal cortex. Given that the temporal cortex in rodents, including the piriform, insular,
104 and entorhinal cortex, is involved in various types of cognitive processes [12-14],
105 establishing large-scale recording techniques covering the parietal to temporal parts of
106 cortices would increase understanding of network dynamics underlying normal cognitive
107 functions and their disruption in diseases.

108 The μECoG device with high-density multi-channel electrodes and fabricated by
109 semiconductor technology enables the simultaneous recording of local field potentials
110 (LFPs) from multiple regions in cerebral cortex with high spatiotemporal resolution [15-
111 17]. The sheet-shaped μECoG device which has been developed using parylene C to
112 reduce sheet thickness, has improved electrode adhesiveness to the curved surface of the
113 brain[6]. Thinning of the sheet-shaped electrodes reduces stiffness and enhances electrode
114 contact to the subject [18]. It has been shown that a relatively thick sheet of μECoG
115 electrode array can be implanted into the cerebral cortex through a small slit on the
116 parietal bone [17, 18]. The electrode arrays make good contact with the brain surface due
117 to compression pressure between the brain and skull, despite adopting the relatively thick

118 sheet in the electrode array. Previous experiments have improved μECoG techniques in
119 order to mitigate anatomical and environmental factors that hinder electrophysiology
120 recordings from cortical regions. Whereas μECoG techniques have the potential to
121 provide a more large-scale neural recording system, a method that covers the parietal and
122 temporal cortex in rodent models has not been developed.

123 The goal of this study is to develop a sheet-shaped μECoG device that is
124 implantable into the epidural space, and to establish the optimal surgical procedures to
125 record from the multisensory regions in temporal cortex. From calculations on the
126 bending stiffness of the μECoG sheet, we showed that the thickness, width, and channel
127 number of metal wiring are key factors for developing μECoG parylene-based electrode
128 arrays. These arrays can be inserted into the space between the skull and brain for optimal
129 large-scale neural recording. After surgical insertion of the sheet-shaped μECoG device,
130 we used histological methods and CT images to confirm that the position of the sheet tip
131 reached to the most ventral part of cerebral cortex without structural damage to the brain
132 surface. This μECoG device allowed successive LFP recordings along the dorsoventral
133 arc of cerebral cortex in an awake mouse. In addition, we simultaneously recorded neural
134 responses corresponding to somatosensory and odor stimuli from different electrodes
135 placed on the parietal and temporal cortex in anesthetized mice. These results show that

136 the sheet-shaped μECoG permits acquisition of large-scale LFP recordings from the
137 parietal to temporal cortex in mice, including somatosensory and olfactory areas.
138
139
140 **Materials and methods**
141 **Device fabrication**
142 The neural electrode array was fabricated on biocompatible parylene film using
143 a standard semiconductor process (Fig. 1a). First, a thick parylene C film was deposited
144 as a base layer on a Si substrate using a parylene coater (PDS2010, Specialty Coating
145 Systems Inc.). Subsequently, a Ti/ Au (50 nm/200 nm) metal wiring layer, including metal
146 neural electrode array, was deposited on parylene film using an electron beam evaporator
147 (ED-1600, SANVAC Co., Ltd.). The array consists of 64 Ti/Au metal electrodes with an
148 area of 80 × 80 μm^2 in a 32 (300 μm pitch) × 2 (400 or 800 μm pitch) configuration.
149 Limited channel crosstalk from the electrode arrangement was confirmed using an
150 equivalent circuit model (Additional File: Additional Method, Fig. S1). The
151 interconnected metal wiring layer was covered with 1 μm thick parylene film. A focal
152 area of parylene was removed by CF_4 and O_2 plasma gas etching to form apertures on the
153 Ti/Au electrode (RIE-200NL, Samco Inc.). Finally, the electrode array was mounted on a
154 printed circuit board (PCB) with a design of 15.5 mm × 14.3 mm using flip chip bonder

155 (M90, HiSOL, Inc.). The cross-section of the electrode array, which is placed on cerebral
156 cortex, is shown in Fig. 1b.
157
158 **Animals**
159 Native male mice C57BL6/J (Japan SLC, Inc., Shizuoka, Japan) were used at 3–
160 6 months of age. All mice were maintained on a 12 h light/dark cycle (lights on 7:00 am–
161 7:00 pm) at 24 ± 3 °C and 55 ± 5% humidity, had ad libitum access to food and water, and
162 were housed in a cage with littermates until surgery.
163
164 **Surgical implantation of the flexible μECoG sheet**
165 Male mice (n = 5, 31.1 ± 2.1 g) were implanted with μECoG arrays in the left
166 cranial hemisphere. During surgery, mice were anesthetized with 0.75 mg/kg
167 medetomidine hydrochloride, 4.0 mg/kg midazolam, and 5.0 mg/kg butorphanol tartrate
168 for recordings under awake conditions, or urethane (1.2 g/kg) for recordings under
169 anesthetized conditions. Mice were placed into a stereotaxic frame (Narishige, Tokyo,
170 Japan) and on a heating pad to maintain normal body temperature (37 °C; MK-900,
171 Muromachi Kikai, or ATC-TY, Unique-Medical Inc., Tokyo, Japan) during surgery. An
172 incision was made in the scalp along the midline of the brain. After exposing the skull, a

173 tendon of temporalis muscle connecting to the edge of parietal bone was cut to secure a
174 space to perform implantation of the μECoG array (Fig. 1c-j). Four stainless steel anchor
175 screws (AN-3, Eicom, Kyoto, Japan) were attached to the skull for mechanical support;
176 one screw was placed on the frontal bone and one on the parietal bone, while the
177 remaining screws, which served as ground and reference, were inserted into the
178 interparietal bone above cerebellum (Fig. 1d). Before the craniotomy, dental acrylic
179 (UNIFAST III, GC Corporation, Tokyo, Japan) was placed on the edge of the exposed
180 skull to affix screws and to protect ground and reference wires (Fig. 1e). The skull was
181 drilled into a rectangular shape from bregma to lambda on the anteroposterior axis and
182 from the right parietal bone to the left squamosal bone on the mediolateral axis (Fig. 1f,
183 approx. 4.5 mm × 6 mm (anteroposterior axis × mediolateral axis)). The surgical
184 procedures ensured preservation of the dura. The head-fixation plate was taped onto the
185 PCB in order to affix it on the head after implantation of the μECoG sheet. A male header
186 pin (TSW-105-20-T-S, DegiKey, USA) was attached to the frontal bone for a device
187 holder, and the μECoG was soldered to secure the PCB onto the skull (Fig. 1g). The
188 μECoG array was carefully inserted into the space between the brain and squamosal bone
189 (Fig. 1h). Note the flexible ECoG sheet was placed on the dura mater. After implantation,
190 the craniotomy site was covered by the parietal bone that was removed during craniotomy,

191 and was embedded using dental acrylic (Fig. 1i). A head-fixation plate, temporarily
192 supported with tape on the PCB, was attached on the head (Fig. 1j, dashed line). After the
193 surgery, mice were placed into a home cage and on a heating pad to maintain body
194 temperature until recordings. Recordings from awake mice were conducted at least 3
195 hours after the completion of surgery. Note that the most important point for successful
196 implantation is to avoid damage to the dura matter. This was achieved by carefully
197 manipulating the drill, tweezer, and device during surgical procedures (Fig. 1f-h).
198

199 **Behavioral task and recordings**

200 Mice were head-fixed on the apparatus and placed in a sound attenuated chamber
201 for the multisensory presentation task. An electrical fan provided background sound (50
202 dB) and ventilation. White LED was placed in front of the right eye, and odor and air
203 tubes were placed in front of the nose and whiskers, respectively. The controller for
204 multisensory presentations was developed using custom programs (LabView, National
205 Instruments, TX). The program pseudorandomly controlled the visual (Frequency, 10 Hz),
206 somatosensory (Flow rate, 2.5 L/min), and odor (Flow rate, 1 L/min, 1% benzaldehyde
207 diluted in mineral oil) stimuli for 3 sec with intertrial intervals (~10–20 sec) that lasted
208 for 100 or 150 trials in the awake or in the anesthetized experiment, respectively (50 trials

each stimulus).

LFP and event signals were recorded at a sampling rate of 20 kHz using the Open Ephys recording system (www.open-ephys.org). Data were downsampled to 1,250 Hz for analysis. Neural signals were amplified on the 64-Channel head stage (C3325, Intan Technologies, USA). To connect the μECoG device and the head stage, a custom-made adapter corresponding to both the flexible flat cable connector (39FVXS-RSM1-GAN-TF, J. S. T. MFG. Co., Ltd, Japan) on the device and the nano strip connectors on the head stage (C3315, Omnetics, USA) was used. Data were analyzed using MATLAB software (MathWorks, MI, USA). The stimulus-evoked LFP was obtained by averaging the LFPs against stimulus onset across trials. To identify sensory stimulus-evoked LFPs on active channels, we compared the peak LFP amplitudes between the before (-600 to 0 ms) and after (0 to 600 ms) stimulus for each electrode. To compare the LFP amplitude between the different electrodes or stimuli, we also used the peak LFP amplitudes for 0.6 sec after stimulus onset. To avoid issues caused by the current transmitting far from the μECoG device, we obtained the profiles of LFPs (LFP profile) by calculating the second spatial derivative of the LFPs [19, 20]. The second spatial derivative is approximated by

$$LFP\ profile(n) = -\frac{\partial^2 \phi(n)}{\partial x^2} \approx -\frac{\phi(n+1) - 2\phi(n) + \phi(n-1)}{(\Delta x)^2}$$

where ϕ is the LFP, Δx is the distance between adjacent electrodes of the μECoG device,

227 and n is the electrode number. The electrode position with a larger LFP profile amplitude
228 indicates the location with a higher current flow than the surrounding regions, indicating
229 that the neural activity near the electrode with a higher LFP profile is high. The LFP
230 profile was calculated using the MATLAB script written by Timothy Olsen (2022)
231 (https://www.mathworks.com/matlabcentral/fileexchange/69399-current-source-density-
232 csd).
233

234 **Histological analysis**

235 After the μECoG implantation and recordings, mice were deeply anesthetized
236 with 5% isoflurane and an overdose of pentobarbital solution, and then transcardially
237 perfused with 0.9% saline. To check the position of the μECoG sheet, the head was cut,
238 and the muscles surrounding the skull were removed using a bone rongeur. The skull was
239 quickly covered in crushed dry ice for flash-freezing. The frozen skull was stored at -
240 30 ℃ until use. To prepare sections including brain, skull, and the flexible μECoG sheet,
241 we used a polyvinylidene chloride film and a modification of a previously described
242 method [21]. The skulls were embedded in OCT compound at −20°C for at least 20 min
243 before slicing in the cryostat. After reaching to the sampling coordinates, the coronal
244 surface of the brain was covered by transfer film (Cryofilm type Ⅱ C(9), SECTION-LAB,

245 Hiroshima, Japan) to avoid detaching the skull, brain, and μECoG sheet from samples.
246 Samples were cut at 30 μm. Serial sections were placed on glass slides (Matsunami, Osaka,
247 Japan) and stained with 4',6-diamidino-2-phenylindole (DAPI; D9542, Sigma-Aldrich,
248 St. Louis, MO) for 5 min. Sections were rinsed by phosphate buffered saline for 3 min
249 and allowed to dry for 20 min. The films containing the sections were flipped onto a drop
250 of embedding agent (ProLong antifade reagents, Thermo Fisher Scientific, USA) on a
251 new glass slide and gently pushed with a finger to adhere them to the substrate. The
252 redundant embedding agent was removed by filter paper, and the perimeter of the film
253 was covered with manicure to prevent tissue drying. Sections were scanned using a BZ-
254 X700 (Keyence, Osaka, Japan) with 4 × objective lens. The contrast and color balance of
255 images scanned under bright field and UV light conditions were adjusted using Photoshop
256 (CC, Adobe Inc., USA). The images were superimposed for analysis.
257
258 **CT imaging**
259 To visualize the position of the μECoG electrode array without removing the
260 skull, we used CT scans (Cosumo Scan Fx, Rigaku Corp., Tokyo Japan). After recordings,
261 mice were perfused with 0.9% saline as described under histological analysis. The PCB
262 of the μECoG and header pin were removed from the head of mice, and the remaining

263 ECoG sheet was bonded to the skull to avoid displacement of the electrode position. The
264 CT data were obtained using the following parameters; tube voltage, 90 kV; tube current,
265 88 μA; exposure time, 2 min; and resolution 20 μm isotropic.
266
267 **Statistics**
268 Statistical analysis was performed using MATLAB software. Comparison of data
269 between two groups was performed using the Student's *t*-test (paired), the Wilcoxon
270 signed rank test (paired), and the Wilcoxon rank-sum test (unpaired). Comparison of data
271 between three groups were constructed using a one-way repeated measures ANOVA or
272 the Friedman test (without assuming normal distribution and homogeneity of variances).
273 The level of statistical significance for variables was set at *$p < 0.05$, **$p < 0.01$, ***$p <$
274 0.001, †$p < 0.05$, †††$p < 0.001$. All statical tests were two-sided.
275
276
277 **Results**
278 **Device fabrication**
279 The thickness of the film is an important factor of stiffness for proper device
280 insertion into the epidural space between the temporal cortex and skull. Devices with

281 different thicknesses were fabricated to understand the effect of parylene thickness on the
282 self-supporting characteristics. The parylene thicknesses T_p of the devices prepared in this
283 study were 7, 13, and 23 μm. Fig. 2a shows photographs of the neural electrode array
284 device with different thicknesses, including optical micrographs of the electrode array.
285 The thin device was curled up owing to strain caused by the thermal expansion coefficient
286 between metal and parylene. As increased thickness of the film results in increased
287 bending stiffness, the thick device was not as curled, but resulted in more robust self-
288 supporting characteristics relative to the thin device. The bending stiffness S of the
289 parylene film without metal can be expressed as

290 $$S = \frac{1}{12} E_p b T_p^3 \qquad (1)$$

291 where E_p and b are the Young's modulus (E_p = 2.78 GPa) and the width (b = 3.1 mm) of
292 parylene film, respectively. It can be seen that S increases rapidly with increasing the T_p.
293 The actual device contains 64 channel Ti/Au metal wiring layer with a high Young's
294 modulus, which affects S. The structured-corrected S was theoretically calculated based
295 on a previous report [22]. Fig. 2b shows the calculated bending stiffness of the device
296 with and without the metal wiring layer as a function of the parylene thickness. The S of
297 the device with the metal layer is ~1.3–1.4 times higher than that of the device without
298 the metal layer. To determine the optimal device design, the thickness and width for

299 parylene, and also the thickness, width, and number of metal wire channels were key
300 factors. Fig. 2c shows the frequency dependence of impedance from a representative
301 neural electrode. Impedances at 1 kHz were approximately 0.5 MΩ. The distribution of
302 channel impedance from the electrode used in the recording experiment in an awake
303 mouse (Fig. 4) is shown in Fig. 2d (0.46 ± 0.07 MΩ). All the devices used (Fig. 5)
304 showed similar impedance characteristics.
305
306 **Histological validation of μECoG sheet position**
307 To examine whether the 23 μm flexible μECoG sheet appropriately reaches to
308 the ventral parts of temporal cortex along the curved surface of mouse cerebral cortex,
309 we histologically validated the position of the μECoG sheet by using adhesive transfer
310 film to prevent the samples from separating [23] (Fig. 3a, see methods). Briefly, we
311 prepared sections including brain, skull, and μECoG sheet and took microscopic images
312 under conditions for bright field and DAPI (nuclear staining). The results showed that the
313 μECoG sheet was situated along the surface of cerebral cortex (Fig. 3a, black arrows),
314 and the tip of the μECoG sheet approached the piriform cortex, which is the most ventral
315 part of the temporal cortex (Fig. 3a, red arrows). In addition, comparisons between
316 ipsilateral and contralateral hemispheres showed no obvious damage in either the dorsal

317 or ventral parts of the cerebral cortex that may have resulted from the surgical procedures
318 required for device insertion (Fig. 3b-d).
319
320 **LFP Recordings in an awake mouse**
321 First, we tested whether the μECoG electrode arrays, implanted onto the
322 temporal cortex by our surgical methods, can monitor LFPs from a broad cortical area of
323 an awake and head-fixed mouse, while also recording sensory stimulus-evoked potentials.
324 Half of the electrodes on the μECoG sheet were inserted into the space between the
325 temporal cortex and skull, and the remaining electrodes were situated on the parietal part
326 of cortex (Fig. 4a). The location of the μECoG sheet in the temporal cortex was confirmed
327 by a CT imaging after the experiment, and the tip of the sheet reached to the most ventral
328 part of the temporal cortex (Fig. 4b), which is comparable with the histological
329 assessment (Fig. 3a). Histological and CT assessments indicated that our μECoG
330 electrodes were placed on parietal to temporal cortices, including the barrel and piriform
331 cortices. Under this condition, we recorded LFPs with the μECoG electrode arrays (Fig.
332 4c) along with the dorsoventral axis of the cortex. Representative LFPs recorded by
333 successive thirty-two electrodes are shown in Fig. 4d. The recording condition was
334 reliably maintained for at least 3 hours under the acute experimental condition.

335 Next, we conducted a sensory cue-presentation task to record cortical potentials
336 responding to sensory stimuli (Fig. 4e). In this experiment, we applied a tactile stimulus
337 to the vibrissa in the form of mild air flow because the ECoG electrode arrays easily target
338 the barrel cortex. The visual stimulus was used as a control stimulus as no electrodes were
339 placed on the visual cortex, which is located in a more posterior region than the barrel
340 cortex. Sensory stimuli were pseudorandomly presented to the mouse every ~10–20 sec.
341 The tactile stimulus induced strong tactile-evoked LFPs in the electrodes placed over the
342 parietal region of the cortex, whereas the visual stimulus did not induce changes in the
343 LFPs recorded from all channels (Fig. 4f). To examine the response characteristics to
344 sensory stimuli on the same channel or between separated channels, we compared the
345 amplitudes of maximal responses of another sensory stimulus and different electrodes to
346 the tactile stimulus. We confirmed that channel 58 showed the maximal change in tactile
347 stimulus-evoked LFP (Fig. 4g, Wilcoxon signed-rank test, $Z = 6.009$, $p < 0.001$, for
348 comparison with baseline amplitudes), which was significantly higher than that of visual
349 stimulus-evoked LFPs (Fig. 4g, Wilcoxon signed-rank test, $Z = 6.087$, $p < 0.001$).
350 Moreover, we confirmed that the peak amplitudes of tactile stimulus-evoked LFP at
351 channel 58 was significantly higher than that of channel 33 (Fig. 4h, Wilcoxon rank-sum
352 test, $Z = 5.112$, $p < 0.001$), the most ventral electrode. To exclude the effects of currents

353 originating far from the μECoG electrodes, we calculated the LFP profiles (see Method).
354 The location of the largest sensory-evoked potential (Fig. 4f) and the largest LFP profile
355 amplitude overlapped at channels surrounding channel 58, indicating that the surrounding
356 region of channel 58 was highly active when the tactile stimulus was applied (Fig. 4i).
357

358 **LFP recordings in anesthetized mice**

359 We tested whether the μECoG electrode array covering the parietal to temporal
360 cortices can monitor cortical activity corresponding to multiple sensory stimuli. In this
361 experiment, we conducted a sensory cue-presentation task that added an odor stimulus to
362 the previous task that used tactile and visual stimuli (Fig. 5a). The neural recordings were
363 carried out under urethane anesthesia because sniffing or chowing behaviors were
364 frequently observed in mice not habituated to the novel odors of the task environments.
365 As shown in Fig. 4a, approximately half of the electrode array on the μECoG sheet were
366 inserted into the epidural space between the temporal cortex and skull, while the other
367 electrodes were placed on the parietal cortex (Fig. 5b).

368 Representative LFP data were recorded by the μECoG electrode arrays from a
369 wide area of cerebral cortex. Before the sensory cue-presentation task, we confirmed the
370 presence of cortical LFPs from parietal to temporal cortices under anesthetized conditions

371 (Fig. 5c, representative LFP). In the sensory cue-presentation task, tactile, odor, and visual
372 stimuli were presented to the mouse pseudorandomly 50 times for each sensory modality
373 (150 times total), every ~10-20 sec. We observed clear tactile and odor stimulus-evoked
374 LFPs from electrodes located on both parietal (Ch. 58 and 62) and temporal (Ch. 33 and
375 37) cortices, respectively (Fig. 5c, averaged LFP). Sensory stimulus-evoked LFPs were
376 not observed from the electrode placed on the middle position of the recording areas along
377 the dorsoventral axis (Ch. 15). We next measured the maximal amplitudes of the sensory
378 stimulus-evoked LFP responses to the tactile, odor, and visual stimuli (50 trials each) in
379 four mice. In channels placed on the parietal cortex, the tactile stimulus induced
380 significantly higher evoked LFP amplitudes relative to the baseline amplitudes that were
381 recorded just before the stimulus onset (Fig. 5d, Wilcoxon signed-rank test, $Z = 4.609$, p
382 < 0.001 for Mouse #1, $Z = 3.595$, $p < 0.001$ for Mouse #2, $Z = 6.042$, $p < 0.001$ for Mouse
383 #3, $Z = 4.581$, $p < 0.001$ for Mouse #4). The tactile stimulus did not result in higher
384 evoked LFP amplitudes than visual and odor stimuli in the same channels in one mouse
385 (Fig. 5d; Friedman test, $\chi^2 = 1.12$, $p = 0.571$, for Mouse #1). In another mouse, the
386 amplitudes evoked by the tactile stimulus were significantly higher than those evoked by
387 the visual stimulus (Fig. 5d; one-way repeated ANOVA, $F(2,147) = 4.86$, $p < 0.01$, *post*
388 *hoc* Tukey–Kramer test, tactile vs. odor, $p = 0.805$, tactile vs. visual, $p < 0.01$, odor vs.

visual, p = 0.052, Mouse #2). In the remaining two mice, the tactile stimulus evoked higher amplitudes relative to the other stimuli (Fig. 5d; Friedman test, χ^2 = 39.04, p < 0.001, *post hoc* Tukey–Kramer test, tactile vs. odor, p < 0.001, tactile vs. visual, p < 0.001, odor vs. visual, p = 0.916 for Mouse #3; χ^2 = 14.68, p < 0.001, *post hoc* Tukey–Kramer test, tactile vs. odor, p < 0.01, tactile vs. visual, p < 0.01, odor vs. visual, p = 0.916 for Mouse #4). The amplitudes of odor stimulus-evoked LFP recordings from channels located on the ventral parts of the temporal cortex were significantly higher than the baseline amplitude in three mice, but not in one mouse (Mouse #3) (Fig. 5e; Wilcoxon signed-rank test, Z = 3.464, p < 0.001 for Mouse #1, Z = 5.146, p < 0.001 for Mouse #2; paired Student's t-test, $t_{(49)}$ = 2.471, p < 0.05 for Mouse #4). In the three mice, the odor-evoked LFP amplitudes tended to be higher than other stimuli-evoked LFP amplitudes (Fig. 5e). Two of the mice showed that the odor stimulus-evoked amplitudes were larger than either the visual or tactile-evoked LFP amplitudes (Fig. 5e; Friedman test, χ^2 = 8.32, p < 0.05, *post hoc* Tukey–Kramer test, tactile vs. odor, p = 0.112, tactile vs. visual, p = 0.703, odor vs. visual, p < 0.05 for Mouse #1; χ^2 = 6.28, p < 0.05, *post hoc* Tukey–Kramer test, tactile vs. odor, p < 0.05, tactile vs. visual, p = 0.514, odor vs. visual, p = 0.341 for Mouse #4). On the other hand, the remaining mouse exhibited odor stimulus-evoked amplitudes that were larger than either the visual or tactile-evoked LFP amplitudes (Fig.

5e; Friedman test, $\chi^2 = 20.32$, $p < 0.001$, *post hoc* Tukey–Kramer test, tactile vs. odor, $p < 0.001$, tactile vs. visual, $p = 0.978$, odor vs. visual, $p < 0.001$ for Mouse #2).

Discussions

EEG and ECoG recordings in humans and non-human primates are used to record neural activity from a wide area of cerebral cortex, including the temporal lobe, with high temporal and spatial resolution [24, 25]. However, there are no techniques to record from the temporal cortex using these techniques in rodents. Such a techniques would provide a powerful tool for neuroscience. Here, we describe the development of a novel μECoG electrode array, including surgical techniques for implanting the device into the mouse temporal cortex. We also confirm that large-scale LFP recordings can be obtained from the novel μECoG electrode array. We show that array thickness is a key factor for the usefulness of parylene-based electrodes. Appropriate stiffness of the μECoG sheet-shaped electrode allowed its insertion into the space between the skull and brain surface, while minimizing the invasiveness of the arrays on the mouse cerebral cortex. In addition, the device could reliably assess sensory stimulus-evoked LFPs from the multiple recording sites covering the somatosensory and olfactory cortex both in awake and

425 anesthetized mice. These techniques are suitable for understanding mechanisms relevant
426 to cognitive functions and pathological conditions in which inter-regional network
427 activities are involved.

428 Tissue penetrating neural electrode arrays are the primary method used for in
429 vivo neuronal recordings in rats and mice. However, damages to brain tissue or dura mater
430 cannot be avoided, and glial scar formation can occur around electrode arrays, leading to
431 quality degradation of neural signals [26]. By contrast, sheet-shaped ECoG electrode
432 arrays are less invasive than penetrating electrode arrays. Several groups have developed
433 insertable devices that implant onto the brain surface, beneath the skull [17, 18, 27, 28].
434 Although these techniques enabled neural recordings from a relatively wide area of the
435 cerebral cortex without penetrating the brain and with little surgery-related tissue trauma,
436 the recording areas were limited to the dorsal parts of cerebral cortex in rodents. Our
437 μECoG sheet overcomes this limitation by expanding the area of cortical recordings to
438 other areas. Using CT imaging and histological methods, we confirmed that placement of
439 the μECoG sheet-shaped array covered the area from the somatosensory cortex to the
440 piriform cortex [29] without structural damage to the cortical surface. In addition, odor
441 stimulus-evoked LFPs were observed from electrodes placed on the tip of the array. These
442 results strongly demonstrate that our μECoG can record from a wider area of the mouse

443 cerebral cortex than existing ECoG methods., This novel μECoG method may shed light
444 on neural network interactions between the parietal and temporal cortex in mice.

445 In this study, we characterized the performance of our μECoG device under
446 awake and anesthetized conditions. The next step would be to assess the usefulness of the
447 device under chronic conditions. The μECoG device was fabricated using parylene,
448 which is a biocompatible material. Previous studies have indicated that parylene-based
449 μECoG devices can maintain electric impedance and the quality of chronic recordings for
450 up to two weeks [30]. Additionally, our surgical methods enabled implantation of the
451 electrode array without structural damage to the dura matter or the layered tissue
452 structures of the cerebral cortex (Fig. 3b-d), despite the wide-area craniotomy needed for
453 electrode placement (Fig. 1g, 4a, and 5b). Our results are consistent with those of a
454 previous study describing a methodology for implanting an μECoG device into the space
455 between the brain surface and skull [18]. Together, the characteristics of our device and
456 surgical methods suggest that they can be used in chronic applications. On the other hand,
457 chronically implanted μECoG devices can cause micro-hematomas and result in opaque
458 connective tissue, which can affect normal cortical activity [31]. Further studies should
459 investigate whether the signal quality is maintained several weeks after implanting the
460 μECoG device using our novel methodology.

461 Thickness is correlated with stiffness and is one of the key factors for the
462 development of thin-film biomedical devices that adhere appropriately to the complex
463 curvature of the skin, heart, and brain surface [6, 18, 32]. Stiffness and adhesion are trade-
464 offs that need be considered in thin film development; for instance, a device with high
465 adhesion properties is not appropriate for insertion into narrow spaces such as the epidural
466 space. Indeed, the insertable μECoG was relatively thicker than the ECoG devices
467 reported previously [6], and therefore, it was possible to move the electrodes to the target
468 area in the narrow space between skull and cortex. Furthermore, the recording data
469 obtained by the ECoG device were comparable to those of devices developed previously
470 [16, 33]. This indicates that optimization of thickness and stiffness is important for the
471 development of adequate devices.

472 Brain-machine interfaces (BMIs) and brain-computer interfaces (BCIs) allow
473 interactions between the brain and external devices [34]. These technologies are expected
474 to restore lost function in patients with neurological impairments. The ECoG has the
475 advantage of being less invasive than penetrating types of electrodes. Another advantage
476 is to be more informative than EEG because of the higher spatial resolution [35]. Previous
477 studies reported that the ECoG signals related to sensory and motor information
478 processing are sufficient to decode the movement trajectory of one- to three-dimensional

479 space, and to manipulate a cursor on a computer screen and a robotic arm [36-38]. In
480 addition, readout of higher-order cognitive brain signals is expected to advance cognitive
481 BMI technology [39]. Applying the μECoG to rodents will boost development of the
482 BMIs/BCIs technology because it is easier to apply to rodents than to humans and non-
483 human primates. Given that the temporal cortex in rodents, including the insular and
484 piriform cortices, is involved in decision making processes based on sensory information
485 [12, 40], enlarged recording techniques covering the parietal to temporal parts of cortices
486 in mouse might have potential for the development and implementation of cognitive
487 BMIs.

488 ECoG and μECoG techniques can be employed in humans, non-human primates,
489 and rodents using a similar methodology [6, 24, 25], thus providing physiological data
490 that can be compared across species. However, the measurement area of current μECoG
491 techniques in mice is limited to the relatively small cortical surface area, and currently
492 does not include the temporal and occipital cortex, which are easily addressed in humans
493 and non-human primates. The μECoG device developed here is insertable into the most
494 ventral parts of the epidural space and makes it possible to record cortical activity from
495 the dorsal to ventral cortices of mice, which has previously been difficult to achieve. Our
496 approach extends the possibility of comparing features of ECoG recordings between

497 mouse and human and non-human primates. Therefore, our μECoG device and
498 methodologies could promote translational research by applying them to rodent models
499 of various pathologies. Possibilities include the combination of μECoG recordings with
500 optogenetics to investigate the causes of diseases. In the future, the integration of these
501 genetical tools and large-scale μECoG recordings may help to further elucidate the
502 mechanisms underpinning neuropsychiatric disorders. Indeed, neuropsychiatric disorders
503 of the brain have been traditionally understood as loss or disruption of brain function due
504 to changes in cell function, neurotransmitter systems, or perturbed neuronal connections.
505 Previous reports have reported changes in alpha and theta oscillation in a wide area of the
506 cortex in Alzheimer's disease patients [41, 42]. Additionally, EEG studies have reported
507 impairments in synchronization between gamma and neural oscillations across various
508 cortical region [43-45]. Although several technologies have been developed to record
509 neural activities in a wide area of the brain, μECoG provides better spatial resolution and
510 signal to noise ratio than EEG and functional magnetic resonance imaging. On the other
511 hand, optogenetics have been used to manipulate selectively cell types and neural circuits.
512 Thus, a combination of μECoG and optogenetics could find out principles of diseases by
513 monitoring and by adding manipulation to impaired neural activities of wide area of
514 cortex in order to promote translational research and/or restore neuropsychiatric diseases.

515

516 **Conclusion**

517 In this study, we developed a 64-channel μECoG device covering the parietal to
518 temporal cortex in mice. The novel surgical procedures enable device placement on the
519 piriform cortex, which is the most ventral part of the mouse cerebral cortex. The device
520 recorded stimulus-evoked potential across multiple sensory areas of cerebral cortex along
521 the dorsal-ventral axis. This system will provide opportunities to investigate
522 physiological functions from wider areas of the mouse cerebral cortex than those of
523 existing ECoG techniques.

524

525

526 **Abbreviations:** micro (m)-electrocorticography (mECoG), computed tomography (CT),
527 electroencephalography (EEG), local field potential (LFP), printed circuit board (PCB),
528 4',6-diamidino-2-phenylindole (DAPI)

529

530

531 **Declarations**

532 **Ethics approval and consent to participate**

All animal procedures were approved by the Animal Care and Use Committee of Dokkyo Medical University (approval number, 1339) and carried out in accordance with the guidelines of the National Institutes of Health.

Consent for publication

Not applicable.

Availability of data and materials

All data used in this paper are available upon reasonable request to the corresponding author.

Competing interests

The authors declare that they have no competing interests.

Funding

This work was supported by the JSPS KAKENHI (19K20074, 19J01997, 21K11556, and 21H05244) (to S.S.), the Tochigi Industrial Promotion Center (the Grant-in-Aid for World-Class Technological Research and Development) (to S.S.), the Nakatomi

Foundation (to S.S.), the Dokkyo Medical University, Investigator-Initiated Research Grant (2020-3) (to S.S.), the Dokkyo Medical University, Project Research Grant (2021-06) (to S.S.), the Dokkyo International Medical Education and Research Foundation (to S.S. and N.O.), the JST PRESTO (JPMJPR1885) (to H.S.), the Casio Science Promotion Foundation (to H.S.), the Toyoaki Scholarship Foundation (to H.S.), the Foundation of Public Interest of Tatematsu (to H.S.), the Research Foundation for Opto-Science and Technology (to H.S. and N.O.), the Naito Foundation (to N.O.), the Astellas Foundation for Research on Metabolic Disorders (to N.O.), and the Takeda Science Foundation (to N.O.). The authors declare no conflicts of interest.

Author contributions

S.S., H.S., and N.O. conceived the project. O.F. and M.O. evaluated the characteristics of the μECoG device. S.S. and Y.S. performed the animal experiments. S.S. analyzed the data. M.I., S.N., and T.H. performed the histological experiments. R.K. and S.T. performed the fabrications and its measurements for the μECoG device. H.M. and K.M. supported the developments for behavioral apparatus and systems. F.S. and K.H. scanned CT imaging. S.S., R.K., H.S., and N.O. wrote the manuscript.

Acknowledgments

We thank the Research Center for Laboratory Animals, Dokkyo Medical University for animal maintenance, the Center for Research Collaboration and Support, Dokkyo Medical University for allowing to use the BZ-X700 fluorescence microscope, and S. Fujiki and all members of Division for Memory and Cognitive Function, Dokkyo Medical University for valuable discussions.

578 **References**

579 1. Kramer, M.A. and S.S. Cash, *Epilepsy as a disorder of cortical network*
580 *organization.* The Neuroscientist, 2012. **18**(4): p. 360-372.

581 2. Li, R., et al., *Dynamic cortical connectivity alterations associated with*
582 *Alzheimer's disease: An EEG and fNIRS integration study.* Neuroimage Clin, 2019.
583 **21**: p. 101622.

584 3. Uhlhaas, P.J. and W. Singer, *Abnormal neural oscillations and synchrony in*
585 *schizophrenia.* Nat Rev Neurosci, 2010. **11**(2): p. 100-13.

586 4. Choi, J.H., et al., *High resolution electroencephalography in freely moving mice.*
587 J Neurophysiol, 2010. **104**(3): p. 1825-34.

588 5. Gilad, A. and F. Helmchen, *Spatiotemporal refinement of signal flow through*
589 *association cortex during learning.* Nat Commun, 2020. **11**(1): p. 1-14.

590 6. Khodagholy, D., et al., *NeuroGrid: recording action potentials from the surface*
591 *of the brain.* Nat Neurosci, 2015. **18**(2): p. 310-5.

592 7. Vázquez-Guardado, A., et al., *Recent advances in neurotechnologies with broad*
593 *potential for neuroscience research.* Nature neuroscience, 2020. **23**(12): p. 1522-
594 1536.

595 8. Khodagholy, D., J.N. Gelinas, and G. Buzsaki, *Learning-enhanced coupling*

between ripple oscillations in association cortices and hippocampus. Science, 2017. **358**(6361): p. 369-372.

9. Sheybani, L., et al., *Electrophysiological Evidence for the Development of a Self-Sustained Large-Scale Epileptic Network in the Kainate Mouse Model of Temporal Lobe Epilepsy.* J Neurosci, 2018. **38**(15): p. 3776-3791.

10. Baverstock, H., N.S. Jeffery, and S.N. Cobb, *The morphology of the mouse masticatory musculature.* J Anat, 2013. **223**(1): p. 46-60.

11. Kimura, R., et al., *Reinforcing operandum: rapid and reliable learning of skilled forelimb movements by head-fixed rodents.* J Neurophysiol, 2012. **108**(6): p. 1781-92.

12. Wang, D., et al., *Task-Demand-Dependent Neural Representation of Odor Information in the Olfactory Bulb and Posterior Piriform Cortex.* J Neurosci, 2019. **39**(50): p. 10002-10018.

13. Lee, J.Y., et al., *Dopamine facilitates associative memory encoding in the entorhinal cortex.* Nature, 2021. **598**(7880): p. 321-326.

14. Rogers-Carter, M.M., et al., *Insular cortex mediates approach and avoidance responses to social affective stimuli.* Nat Neurosci, 2018. **21**(3): p. 404-414.

15. Kaiju, T., et al., *High Spatiotemporal Resolution ECoG Recording of*

Somatosensory Evoked Potentials with Flexible Micro-Electrode Arrays. Front Neural Circuits, 2017. **11**: p. 20.

16. Konerding, W.S., et al., *New thin-film surface electrode array enables brain mapping with high spatial acuity in rodents.* Sci Rep, 2018. **8**(1): p. 3825.

17. Yeager, J.D., et al., *Characterization of flexible ECoG electrode arrays for chronic recording in awake rats.* J Neurosci Methods, 2008. **173**(2): p. 279-85.

18. Park, A.H., et al., *Optogenetic Mapping of Functional Connectivity in Freely Moving Mice via Insertable Wrapping Electrode Array Beneath the Skull.* ACS Nano, 2016. **10**(2): p. 2791-802.

19. Mitzdorf, U., *Current source-density method and application in cat cerebral cortex: investigation of evoked potentials and EEG phenomena.* Physiol Rev, 1985. **65**(1): p. 37-100.

20. Buzsáki, G., C.A. Anastassiou, and C. Koch, *The origin of extracellular fields and currents—EEG, ECoG, LFP and spikes.* Nature reviews neuroscience, 2012. **13**(6): p. 407-420.

21. Kawamoto, T., *Use of a new adhesive film for the preparation of multi-purpose fresh-frozen sections from hard tissues, whole-animals, insects and plants.* Arch Histol Cytol, 2003. **66**(2): p. 123-43.

632 22. Kim, D.H., et al., *Dissolvable films of silk fibroin for ultrathin conformal bio-*
633 *integrated electronics.* Nat Mater, 2010. **9**(6): p. 511-7.
634 23. Kawamoto, T. and M. Shimizu, *A method for preparing 2-to 50-µm-thick fresh-*
635 *frozen sections of large samples and undecalcified hard tissues.* Histochem Cell
636 Biol, 2000. **113**(5): p. 331-339.
637 24. Kaneko, T., et al., *Cortical neural dynamics unveil the rhythm of natural visual*
638 *behavior in marmosets.* Commun Biol, 2022. **5**(1): p. 108.
639 25. Wang, W., et al. *Human motor cortical activity recorded with Micro-ECoG*
640 *electrodes, during individual finger movements*. in *Conf Proc IEEE Eng Med Biol*
641 *Soc*. 2009. IEEE.
642 26. Kotov, N.A., et al., *Nanomaterials for neural interfaces.* Adv Mater, 2009. **21**(40):
643 p. 3970-4004.
644 27. Hollenberg, B.A., et al., *A MEMS fabricated flexible electrode array for recording*
645 *surface field potentials.* J Neurosci Methods, 2006. **153**(1): p. 147-53.
646 28. Jeong, U.J., et al., *A minimally invasive flexible electrode array for simultaneous*
647 *recording of ECoG signals from multiple brain regions.* Lab Chip, 2021. **21**(12):
648 p. 2383-2397.
649 29. Franklin, K. and G. Paxinos, *The Mouse Brain in Stereotaxic Coordinates 3rd edn*

(New York: Academic). 2007.

30. Toda, H., et al., *Simultaneous recording of ECoG and intracortical neuronal activity using a flexible multichannel electrode-mesh in visual cortex.* Neuroimage, 2011. **54**(1): p. 203-12.

31. Schendel, A.A., et al., *A cranial window imaging method for monitoring vascular growth around chronically implanted micro-ECoG devices.* J Neurosci Methods, 2013. **218**(1): p. 121-30.

32. Park, S., et al., *Self-powered ultra-flexible electronics via nano-grating-patterned organic photovoltaics.* Nature, 2018. **561**(7724): p. 516-521.

33. Alahi, M.E.E., et al., *Recent advancement of electrocorticography (ECoG) electrodes for chronic neural recording/stimulation.* Mater Today Commun, 2021. **29**: p. 102853.

34. Lebedev, M.A. and M.A. Nicolelis, *Brain-Machine Interfaces: From Basic Science to Neuroprostheses and Neurorehabilitation.* Physiol Rev, 2017. **97**(2): p. 767-837.

35. Volkova, K., et al., *Decoding Movement From Electrocorticographic Activity: A Review.* Front Neuroinform, 2019. **13**: p. 74.

36. Hochberg, L.R., et al., *Reach and grasp by people with tetraplegia using a*

neurally controlled robotic arm. Nature, 2012. **485**(7398): p. 372-5.

37. Flesher, S.N., et al., *A brain-computer interface that evokes tactile sensations improves robotic arm control.* Science, 2021. **372**(6544): p. 831-836.

38. Birbaumer, N., et al., *A spelling device for the paralysed.* Nature, 1999. **398**(6725): p. 297-8.

39. Min, B.K., R. Chavarriaga, and J.D.R. Millan, *Harnessing Prefrontal Cognitive Signals for Brain-Machine Interfaces.* Trends Biotechnol, 2017. **35**(7): p. 585-597.

40. Vincis, R., et al., *Dynamic Representation of Taste-Related Decisions in the Gustatory Insular Cortex of Mice.* Curr Biol, 2020. **30**(10): p. 1834-1844 e5.

41. Cecchetti, G., et al., *Resting-state electroencephalographic biomarkers of Alzheimer's disease.* Neuroimage Clin, 2021. **31**: p. 102711.

42. Spinelli, G., et al., *Theta Band-Power Shapes Amyloid-Driven Longitudinal EEG Changes in Elderly Subjective Memory Complainers At-Risk for Alzheimer's Disease.* J. Alzheimer's Dis., 2022(Preprint): p. 1-16.

43. Canuet, L., et al., *Resting-state EEG source localization and functional connectivity in schizophrenia-like psychosis of epilepsy.* PLoS One, 2011. **6**(11): p. e27863.

44. Wynn, J.K., et al., *EEG findings of reduced neural synchronization during visual*

686 *integration in schizophrenia.* PLoS One, 2015. **10**(3): p. e0119849.

687 45. Steinmann, S., et al., *Auditory verbal hallucinations related to altered long-range*

688 *synchrony of gamma-band oscillations.* Sci Rep, 2017. **7**(1): p. 8401.

689

690

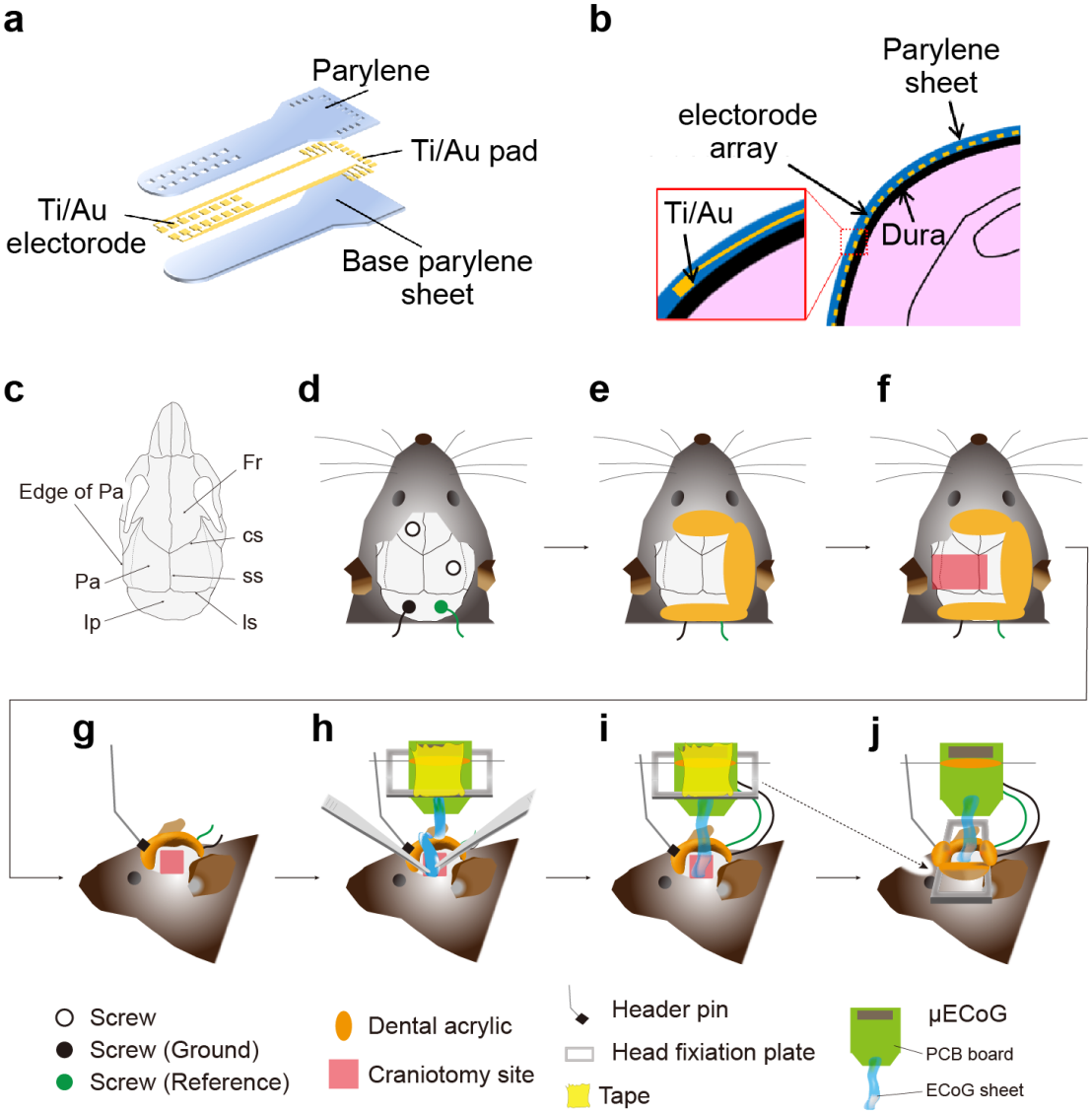

Fig. 1. Surgical procedures for the placement of the sheet-shaped μECoG device. (a) A schematic of the device showing its various components. (b) Schematic representation of a cross-section of the neural electrode array device placed on the cerebral cortex. (c) The cranial sutures in the dorsal view, Fr, Frontal bone; IP, Interparietal bone; Pa, parietal bone; cs, coronal suture; ss, sagittal suture; ls, lambdoid suture; edge of Pa, the edge of parietal bone connecting the temporalis muscle. (d-j) Schematic representations of the

698 surgical procedures for inserting the μECoG electrode array into the space between the

699 brain and skull.

700

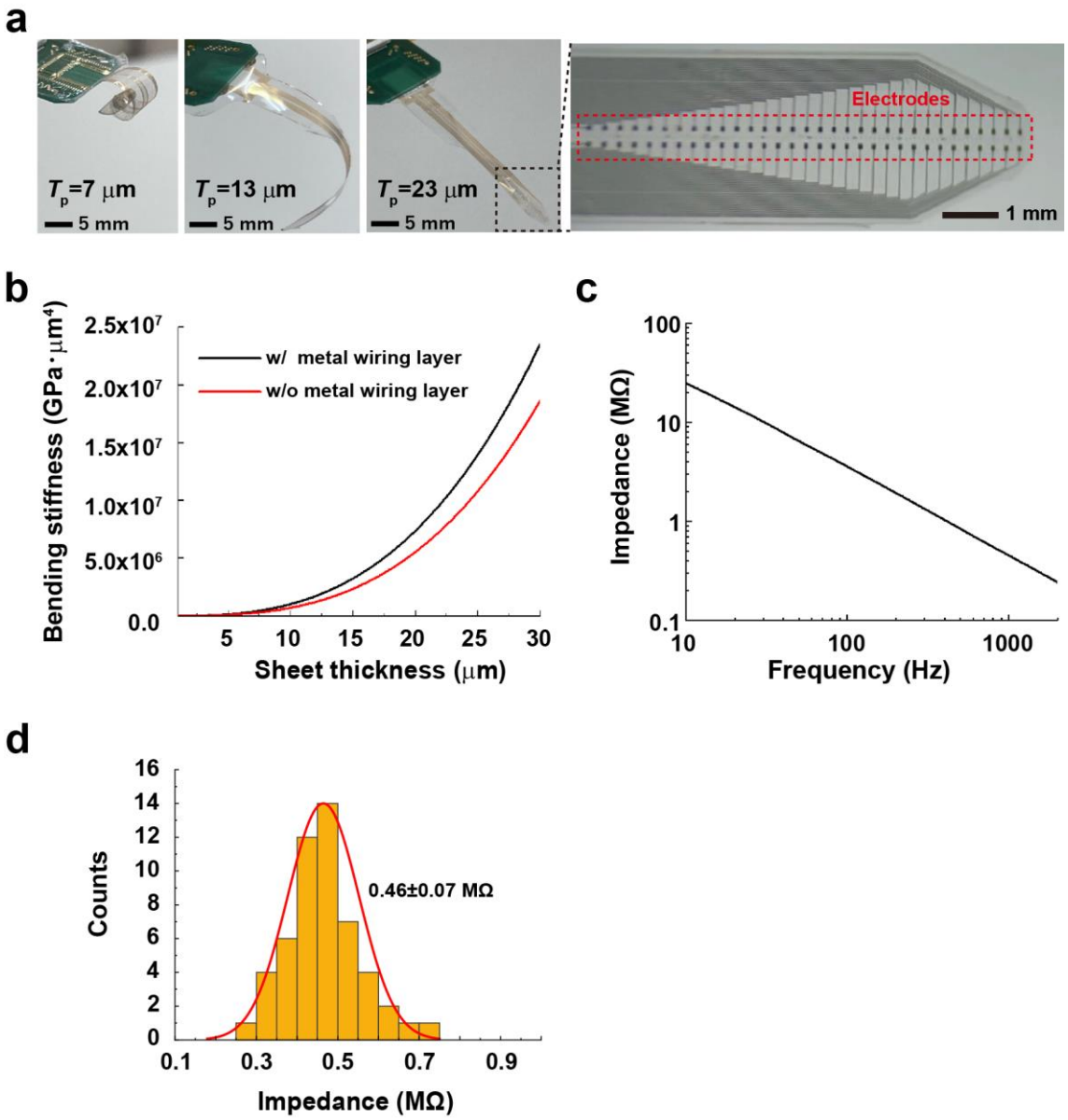

Fig. 2. Bending stiffness of the sheet-shaped μECoG device. (a) Photographs of a μECoG sheet with different parylene thicknesses of 7, 13, 23 μm and an optical microscope image of a sheet with arranged neural electrodes (Ti/Au). While the 7 μm thick sheet strongly curls, the 23 μm thick sheet has high self-supporting characteristics. (b) Calculated bending stiffness of the device with and without the metal wiring layer as a function of

the parylene thickness. (c) Frequency dependence of impedance of the representative neural electrode. The impedance at 1 kHz was approximately 0.5 MΩ. (d) The distribution of impedances of μECoG electrodes (52 / 64 channels). The remaining channels were removed due to high impedance (> 5 MΩ).

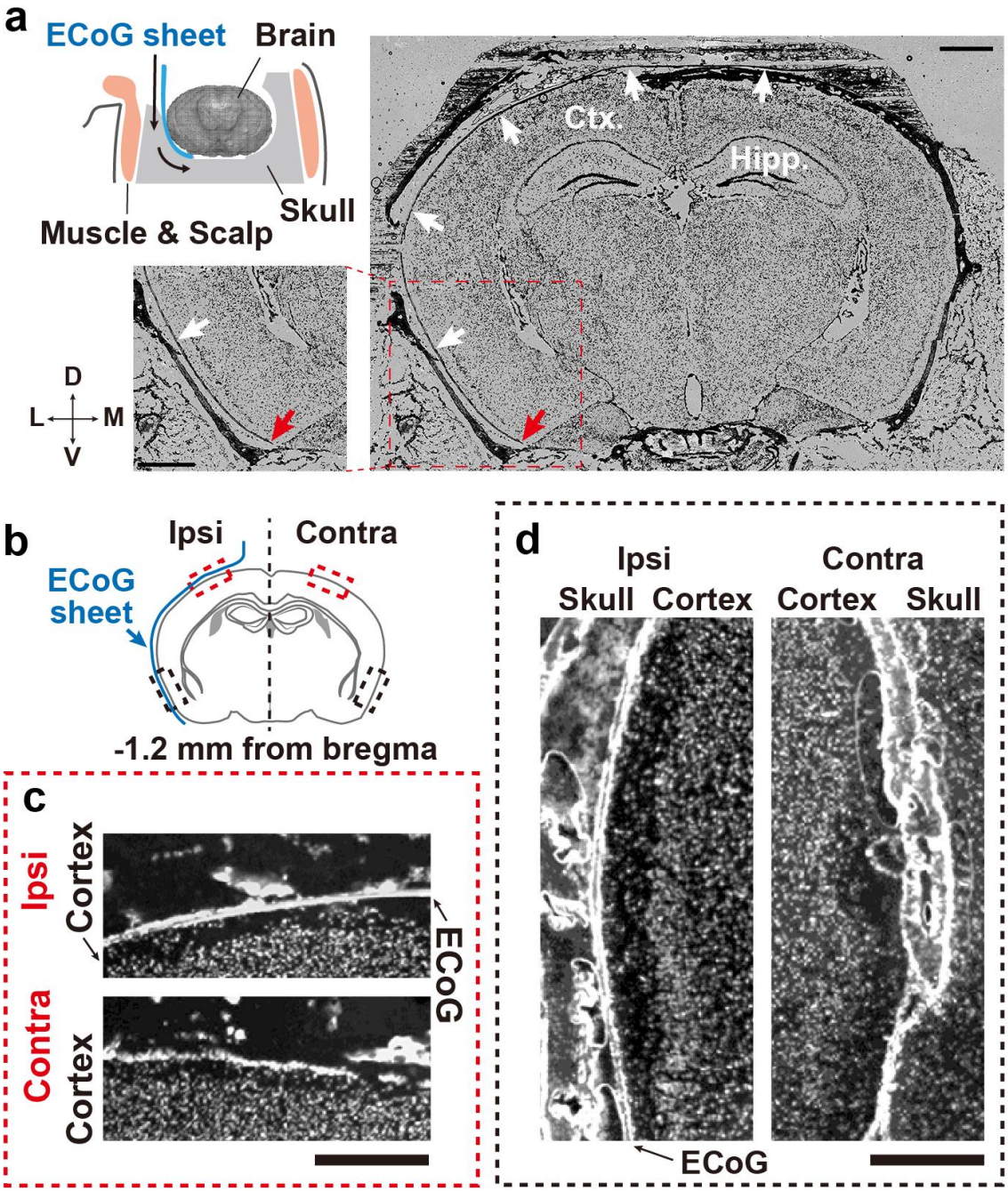

Fig. 3. Histological validation of the μECoG sheet position. (a) A schematic of the position of the μECoG sheet placed on the brain surface (upper left). Superimposed microscopic images of bright field and DAPI staining (right and lower left). Black arrows

717 indicate the μECoG sheet on the brain surface. The insets show enlargements of the
718 dashed rectangle. Red arrows indicate the tip of the μECoG sheet. Scale bars: 1 mm. Ctx,
719 cortex; Hipp, hippocampus; D, dorsal; M, medial; V, ventral; L, lateral. (b-d) Comparison
720 of cortical structure between the μECoG sheet-inserted hemisphere (ipsi-lateral side) and
721 opposite hemisphere (contralateral side). Ipsi, ipsilateral; Contra, contralateral. (b)
722 Schematic drawing of a coronal view of the mouse brain; black and red dashed rectangles
723 indicate the parietal (c) and temporal cortex (d), respectively. Scale bars: 500 μm.
724

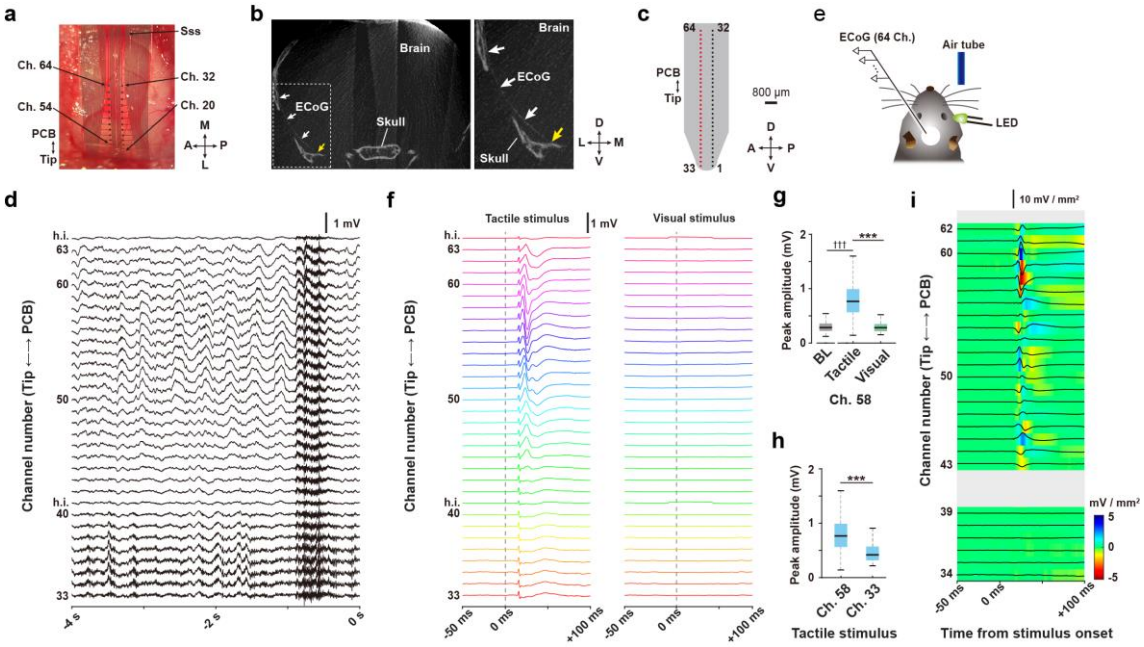

Fig. 4. LFP Recordings by the μECoG sheet electrode in an awake mouse (a) Dorsal view of the μECoG electrode array placed on the parietal cortex. M, medial; L, lateral; A, anterior; P, posterior; Ch., channel of electrode; Sss, superior sagittal sinus. (b) The position of the μECoG sheet placed on the brain surface as revealed by CT scanning. White arrows indicate the μECoG sheet placed on space between the brain and skull. The enlarged image (right) shows the tip of μECoG sheet in the brain (yellow arrow). D, dorsal; V, ventral; M, medial; L, lateral. (c) The 64-channel μECoG electrode array. Numbers are the channel IDs of the electrode. Red rectangles indicate the thirty-two successive electrodes that recorded representative LFPs along the dorsoventral axis of the cortex. D, dorsal; V, ventral; A, anterior; P, posterior. (d) Representative LFPs before the sensory presentation task. Numbers indicate channels of the electrode corresponding to

(c) h.i., channel of high impedance (> 5 MΩ). (e) Schematic drawing of the sensory presentation task and recordings in a head-fixed mouse. (f) Average sensory-evoked LFPs. (g) Averaged peak LFP amplitudes in the same channels elicited by different stimuli. BL, baseline. (h) Averaged peak LFP amplitudes in different channels elicited by the same stimulus. (i) The current source density map calculated from the averaged tactile-evoked LFPs in (f). The central lines and edges of the boxes indicates the median and quartiles, respectively, and whiskers extend to the maximum and minimum. ***$P < 0.001$. ††† < 0.001 vs. baseline amplitude.

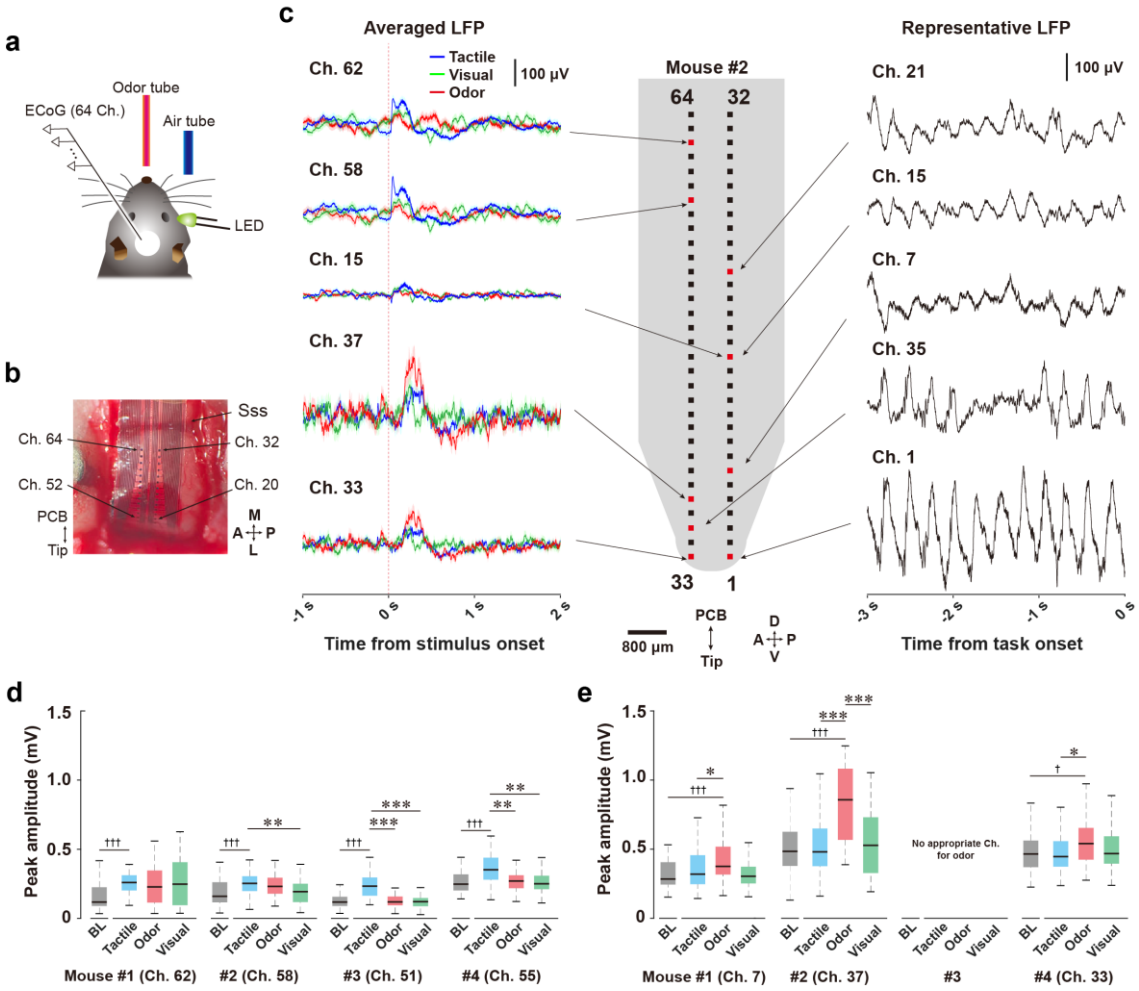

Fig. 5. The μECoG electrode can monitor cortical activities in response to multiple sensory stimuli. (a) Schematic drawing of the sensory presentation task and recordings in a head-fixed mouse. (b) Dorsal view of the μECoG electrode array on the parietal cortex. M, medial; L, lateral; A, anterior; P, posterior; Ch., channel of electrode; Sss, superior sagittal sinus. (c) The 64-channel μECoG electrode array and LFPs at start of the task (representative LFP) or on task (averaged LFP) in a mouse. LFPs corresponding to the tactile, visual, and odor stimuli are indicated as blue, green, and red line, respectively. Shadows indicate SEM. D, dorsal; V, ventral; A, anterior; P, posterior. (d) Averaged peak

LFP amplitudes recorded by the channels in which the maximal change was observed for the tactile stimulus. BL, baseline. (e) Averaged peak LFP amplitudes recorded by the channels in which the maximal change was observed for the odor stimulus. There are no channels showing significant differences between odor stimulus-evoked and baseline LFP amplitudes in the #3 mouse. The central lines and edges of the boxes indicate the median and quartiles, respectively, and whiskers extend to the maximum and minimum with outliers excluded. *$P > 0.05$, ***$P < 0.001$ vs. each stimulus. †$P > 0.05$, ††† < 0.001 vs. baseline amplitude.